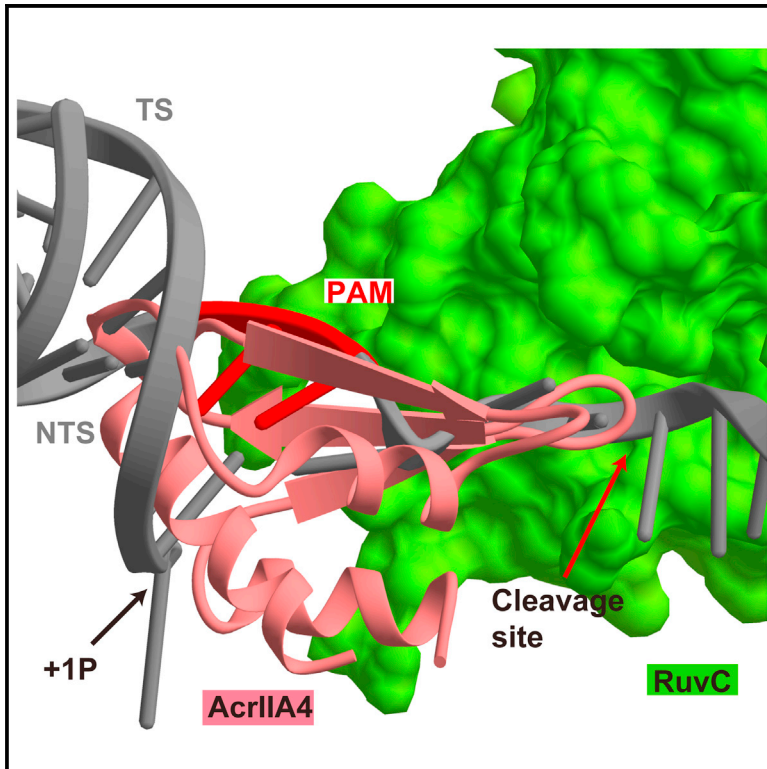


# Inhibition Mechanism of an Anti-CRISPR Suppressor AcrIIA4 Targeting SpyCas9

## Graphical Abstract



## Authors

Hui Yang, Dinshaw J. Patel

## Correspondence

yangh3@mskcc.org (H.Y.),  
pateld@mskcc.org (D.J.P.)

## In Brief

Anti-CRISPRs are phage factors that inhibit bacterial CRISPR systems. Yang and Patel describe the structure of an anti-CRISPR protein, AcrIIA4, in complex with Cas9 with single-guide RNA. The structure reveals the mechanism of inhibition and provides the basis for developing tools to regulate Cas9 function in genome editing.

## Highlights

- Crystal structure of *S. pyogenes* Cas9 in complex with sgRNA and suppressor AcrIIA4
- Selective recognition of pre-target bound SpyCas9 binary complex by AcrIIA4
- Competitive binding of AcrIIA4 over dsDNA for SpyCas9-sgRNA binary complex
- Mechanistic insights into blockage of SpyCas9 preventing dsDNA cleavage by AcrIIA4



# Inhibition Mechanism of an Anti-CRISPR Suppressor AcrIIA4 Targeting SpyCas9

Hui Yang<sup>1,\*</sup> and Dinshaw J. Patel<sup>1,2,\*</sup><sup>1</sup>Structural Biology Program, Memorial Sloan Kettering Cancer Center, New York, NY 10065, USA<sup>2</sup>Lead Contact

\*Correspondence: yangh3@mskcc.org (H.Y.), pateld@mskcc.org (D.J.P.)

<http://dx.doi.org/10.1016/j.molcel.2017.05.024>

## SUMMARY

Prokaryotic CRISPR-Cas adaptive immune systems utilize sequence-specific RNA-guided endonucleases to defend against infection by viruses, bacteriophages, and mobile elements, while these foreign genetic elements evolve diverse anti-CRISPR proteins to overcome the CRISPR-Cas-mediated defense of the host. Recently, AcrIIA2 and AcrIIA4, encoded by *Listeria monocytogenes* prophages, were shown to block the endonuclease activity of type II-A *Streptococcus pyogenes* Cas9 (SpyCas9). We now report the crystal structure of AcrIIA4 in complex with single-guide RNA-bound SpyCas9, thereby establishing that AcrIIA4 preferentially targets critical residues essential for PAM duplex recognition, as well as blocks target DNA access to key catalytic residues lining the RuvC pocket. These structural insights, validated by biochemical assays on key mutants, demonstrate that AcrIIA4 competitively occupies both PAM-interacting and non-target DNA strand cleavage catalytic pockets. Our studies provide insights into anti-CRISPR-mediated suppression mechanisms for inactivating SpyCas9, thereby broadening the applicability of CRISPR-Cas regulatory tools for genome editing.

## INTRODUCTION

In bacteria, defense against phage predation relies on restriction-modification (R-M) systems, as well as CRISPR and CRISPR-associated (CRISPR-Cas) systems (Dupuis et al., 2013; Hille and Charpentier, 2016; Labrie et al., 2010; Marraffini, 2015; Mohanraju et al., 2016; Nishimasu and Nureki, 2017; Wright et al., 2016). The R-M systems provide ubiquitous and innate protection against any invaders not possessing countermeasures. The CRISPR-Cas systems were found in almost all archaea and about 50% of bacteria and function as the only adaptive immune system, which utilizes sequence-specific RNA-guided endonucleases to cut foreign genetic elements. The CRISPR-Cas immunity pathway relies on divergent Cas proteins and CRISPR RNA (crRNA) and can be divided into three

stages: spacer acquisition, crRNA biogenesis, and target interference (van der Oost et al., 2009; Wright et al., 2016). The Cas proteins and crRNA are encoded by the CRISPR locus, which is composed of variable cas genes and a CRISPR array comprising short direct repeats separated by spacers. Based on the phylogenetic classification, the CRISPR-Cas systems can be grouped into two classes and subdivided into 6 types and 19 subtypes: class 1 systems (types I, III, and IV) employ multi-subunit surveillance ribonucleoprotein complexes termed Cascade (CRISPR-associated complex for antiviral defense), while class 2 systems (types II, V, and VI) rely on single effector proteins (Makarova et al., 2011, 2015; Shmakov et al., 2015).

In turn, phages and mobile genetic elements have developed divergent strategies to overcome the immune defense systems in host bacteria, which include adsorption inhibition, abortive infection, R-M systems, and CRISPR-Cas systems (Samson et al., 2013). Recently, a range of phage-encoded “anti-CRISPR” proteins that suppress different CRISPR-Cas systems has been identified. Specially, ten type I-E and four type I-E anti-CRISPR proteins were discovered to inactivate *Pseudomonas aeruginosa* CRISPR-Cas systems (Bondy-Denomy et al., 2013, 2015; Pawluk et al., 2014, 2016b). Four type II-A anti-CRISPR proteins encoded by *L. monocytogenes* prophages were identified, and two of them blocked both *S. pyogenes* Cas9 (SpyCas9) and *L. monocytogenes* Cas9 (Lmo-Cas9) (Rauch et al., 2017). Three families of type II-C anti-CRISPR proteins targeting *N. meningitidis* Cas9 (NmeCas9) have also been reported (Pawluk et al., 2016a). Moreover, a type VI-B anti-Cas13b protein, Csx27, was identified as an inhibitor for both *B. zoohelcum* Cas13b (type VI-B1) and *P. buccae* Cas13b (type VI-B2) systems, while an activator, Csx28 for *P. buccae* Cas13b was also identified (Smargon et al., 2017).

The programmability of CRISPR-Cas systems has been widely developed as a genetic tool and provides immense promise for therapeutic applications (Barrangou and Doudna, 2016; Hsu et al., 2014). Two class 2 CRISPR-Cas effectors, namely Cas9 (type II) (Barrangou and Doudna, 2016; Hsu et al., 2014; Jiang and Marraffini, 2015; Sternberg and Doudna, 2015; Wright et al., 2016) and Cas12a (also known as Cpf1, type V) (Zetsche et al., 2015), that cleave double-stranded DNA (dsDNA) targets have been successfully harnessed for genome editing. Newly identified Cas13a (also known as C2c2, type VI), which cleaves RNA targets (Abudayyeh et al., 2016; East-Seletsky et al., 2016, 2017; Liu et al., 2017), has been developed as a rapid detection tool for diagnosis

of pathogens and genotyping (Gootenberg et al., 2017). Cas9 requires either a pair of RNA molecules, namely crRNA and tracrRNA (*trans*-activating crRNA), or a synthetic single-guide RNA (sgRNA) involving a tetra loop covalently linking the 3' end of crRNA to the 5' end of tracrRNA (Garneau et al., 2010; Gasiunas et al., 2012; Jinek et al., 2012), as well as a short 3'-G-rich proto-spacer adjacent motif (PAM) sequence on the non-target strand proximal to the cleavage site (Deveau et al., 2008; Mojica et al., 2009). Cas9 uses two nuclease domains, namely HNH and RuvC domains, to generate blunt-end double-strand breaks. The HNH domain cleaves the target DNA strand that is base-paired with the crRNA guide, while the RuvC domain cleaves the non-base-paired single-stranded non-target DNA strand (Barangou et al., 2007; Deltcheva et al., 2011; Garneau et al., 2010; Gasiunas et al., 2012; Jinek et al., 2012). To date, SpyCas9 remains the most commonly used and powerful genome-editing tool. Besides, a catalytically dead mutant, SpyCas9 (dSpyCas9, D10A/H840A) has served as an effective and specific RNA-guided genome-binding platform (Dominguez et al., 2016; Qi et al., 2013; Wang et al., 2016a). Although the principles underlying SpyCas9 cleavage specificity are well understood and the technology underlying its commercial applicability is well developed, further knowledge is required to minimize side effects resulting from alternate cleavage patterns, thereby insuring effective and safe genome editing in the clinic. The discovery of anti-CRISPR proteins has provided the prospect of introducing robust, specific, and genetically encodable "off-switch" tools for modulating Cas9 activity. Until very recently, the suppression mechanisms of two reported anti-SpyCas9 proteins, AcrIIA2 and AcrIIA4, which block the activity of SpyCas9 in bacteria and human cells (Rauch et al., 2017), have remained unknown.

To address this goal, we investigated the structural principles underlying the mode of action of these AcrII anti-CRISPR proteins in overcoming CRISPR-Cas-mediated host defense. We observed direct interactions between sgRNA-bound SpyCas9 and AcrIIA4, as well as AcrIIA2. To better understand the inhibition mechanism of AcrIIA4, we determined the crystal structure of AcrIIA4 bound to the SpyCas9-sgRNA binary complex. The structural comparisons reveal that AcrIIA4 preferentially interacts with SpyCas9-sgRNA binary complex and competitively occupies the binding surface for the PAM duplex, as well as blocks non-target strand access to the active site in the RuvC pocket, thereby further contributing to the inactivation of SpyCas9. Our structural studies and biochemical characterization of interfacial mutants for AcrIIA4 bound to sgRNA-bound SpyCas9 provide guidelines for the further development of natural anti-CRISPR off-switch tools for genome engineering and related biotechnology applications.

## RESULTS

### AcrIIA2 and AcrIIA4 Physically Interact with SpyCas9

It has been reported previously that anti-CRISPR protein AcrIIA2 partially blocks dSpyCas9 function in *Escherichia coli*, while AcrIIA4 shows almost completely blockage. Both AcrIIA2 and AcrIIA4 also suppress the Cas9-based genome editing in HEK293T cells (Rauch et al., 2017). We tested for whether AcrIIA2 and AcrIIA4 can suppress SpyCas9 activity for a linear

dsDNA target containing a 5'-TGG-3' PAM sequence in vitro in the presence of an 85-nt sgRNA, as described previously (Jinek et al., 2012). With increasing amount of AcrIIA2 and AcrIIA4, the enzymatic activity of SpyCas9 was blocked in a dose-dependent manner, with AcrIIA4 exhibiting a relatively higher blockage effect (Figure 1A, left panel) than AcrIIA2 (Figure S1A), consistent with reported in vivo data (Rauch et al., 2017). Indeed, availability of sufficient AcrIIA2 and AcrIIA4 results in the complete blockage of the catalytic activity of SpyCas9 (Figure 1A, left panel; Figure S1A), similar to the effect observed for mutations in dSpyCas9 (Figure 1A, right panel).

We then investigated whether AcrIIA2 and AcrIIA4 inactivate SpyCas9 by direct interaction. Previous structural data showed that large conformational changes occur during the transitions between apo-SpyCas9, sgRNA-bound, and dsDNA target-bound states (Anders et al., 2014; Jiang et al., 2015, 2016; Jinek et al., 2014; Nishimasu et al., 2014). We performed size-exclusion chromatography (SEC) to detect whether AcrIIA2 and AcrIIA4 specifically bind to one state or universally to more than one state of SpyCas9 and also whether they form stable complexes with SpyCas9 in solution (Figure 1B; Figure S1B, top panels). To avoid potential cleavage of the target dsDNA, we used dSpyCas9 to generate dsDNA target-bound ternary complex. Notably, in the presence of sgRNA, AcrIIA2 and AcrIIA4 form stable complexes with SpyCas9, whereas no band or very weak bands were detected when using either apo-SpyCas9 or dSpyCas9-sgRNA-dsDNA ternary complex (Figure 1B; Figure S1B, bottom panels).

In addition, AcrIIA2 and AcrIIA4 show strong binding to sgRNA-bound maltose-binding protein (MBP)-SpyCas9 binary complex, while very weak interactions were detected between apo-MBP-SpyCas9 with AcrIIA2 and with AcrIIA4 (Figure 1C, left panel; Figure S1C). Similarly, MBP-AcrIIA4 only shows strong binding to sgRNA-bound SpyCas9, while dsDNA target-bound dSpyCas9-sgRNA shows significantly reduced binding affinity to AcrIIA4 (Figure 1C, right panel). The attachment of an MBP tag at either SpyCas9 or AcrIIA4 has minimal effect on the blockage of enzymatic activity (Figure 1A, right panel). The data outlined in Figures 1B, 1C, S1B, and S1C demonstrate that AcrIIA2 and AcrIIA4 specifically recognize sgRNA-bound rather than either apo or dsDNA target-bound states of SpyCas9.

We analyzed whether AcrIIA2 and AcrIIA4 formed monomers or higher oligomers in the free state in solution by SEC coupled with in-line multi-angle light scattering analysis (SEC-MALLS). The measured molecular masses are close to the theoretical molecular mass for monomers (14.4 kDa versus 14.2 kDa for AcrIIA2 and 10.4 kDa versus 10.2 kDa for AcrIIA4), indicating that AcrIIA2 and AcrIIA4 in the free state exist as monomers in solution (Figure 1D; Figure S1D).

### Structure of SpyCas9-sgRNA-AcrIIA4 Ternary Complex

The color-coded domain architecture of SpyCas9 is shown in Figure 2A, while the color-coded secondary structure of the sgRNA composed of covalently linked crRNA and tracrRNA is shown in Figure S2A. We solved the crystal structure of AcrIIA4 bound to dSpyCas9-sgRNA at 2.6 Å resolution (X-ray statistics summarized in Table 1). SpyCas9 resembles an overall "Crab Claw" fold consisting of an  $\alpha$ -helical recognition (REC) lobe

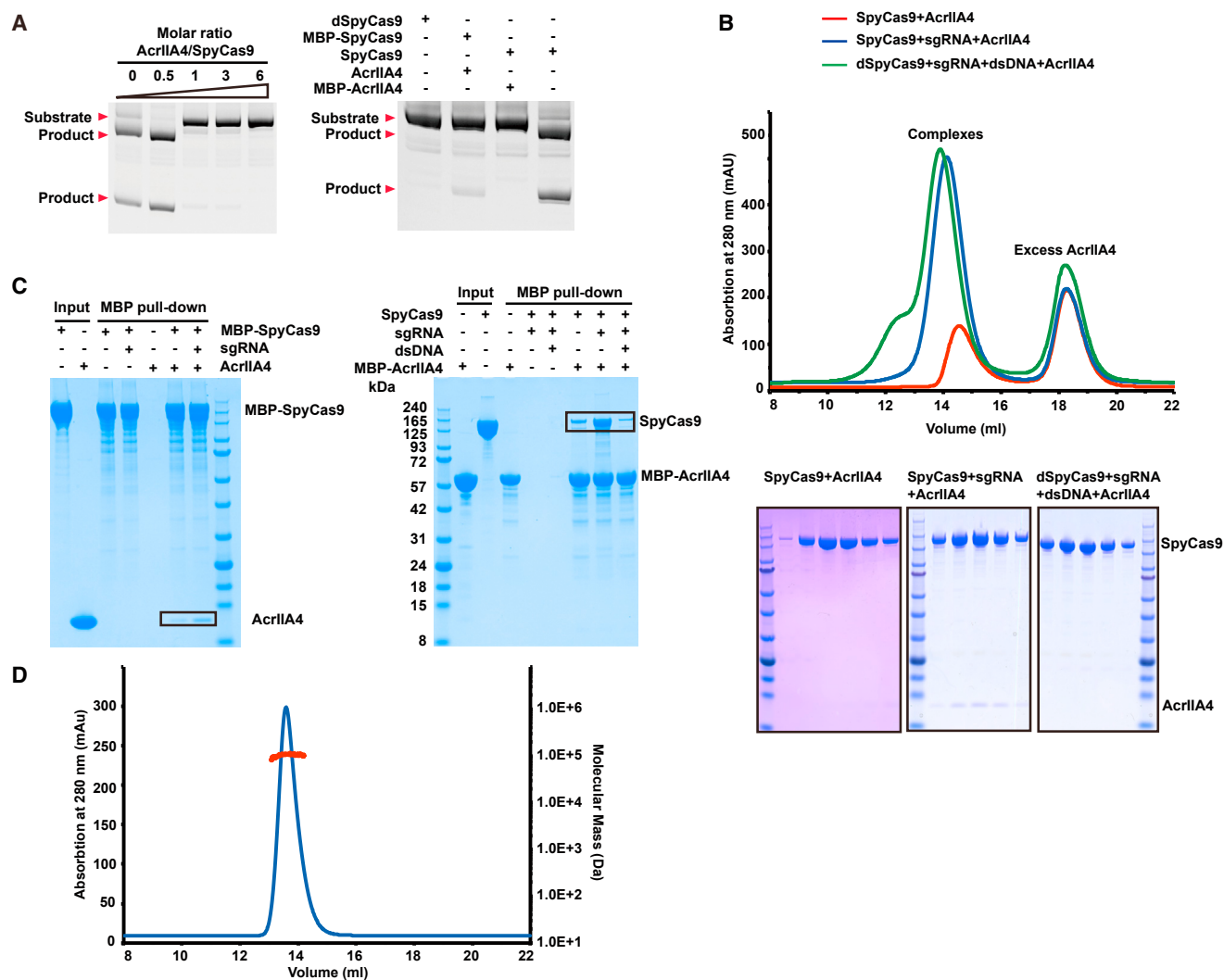


**Figure 1. AcrIIA4 Directly Interacts with sgRNA-Bound SpyCas9 and Inactivates SpyCas9**

(A) *In vitro* enzymatic assay monitoring cleavage of linear dsDNA by SpyCas9 and sgRNA in the presence of AcrIIA4. The molar ratios of AcrIIA4:SpyCas9 are shown at the top of each lanes (left). The inhibition between MBP-tagged SpyCas9 and AcrIIA4 is also detected and compared with dSpyCas9 (right).

(B) AcrIIA4 selectively forms a stable complex with sgRNA-bound SpyCas9 rather than apo or DNA-bound SpyCas9-sgRNA in solution. SEC was performed using SpyCas9 in the presence or absence of sgRNA and sgRNA-dsDNA.

(C) AcrIIA4 physically interacts with sgRNA-bound SpyCas9. MBP pull-down assays were performed using MBP-tagged AcrIIA4 and SpyCas9 in presence or absence of sgRNA and sgRNA-dsDNA.

(D) Oligomeric state of AcrIIA4 in solution detected by SEC-MALS. The horizontal red line represents the SEC-MALS calculated mass for AcrIIA4. The calculated and theoretical molecular masses are 10.4 kDa and 10.2 kDa, respectively, indicating that AcrIIA4 exists as a monomer in solution.

See also Figure S1.

composed of Helical-I and Helical-II domains and a NUC lobe composed of RuvC, HNH, Topo, and CTD domains, as described previously (Figure 2B) (Anders et al., 2014; Jiang et al., 2015, 2016; Jinek et al., 2014; Nishimasu et al., 2014). The arginine-rich bridge helix (BH) motif connects the two lobes. The tertiary fold of the sgRNA in the AcrIIA4-bound ternary complex is shown in Figure S2B. AcrIIA4 is positioned on one face of SpyCas9 formed by Topo, RuvC, and CTD domains, with one AcrIIA4 bound per SpyCas9-sgRNA complex (see circled region, Figure 2B; Figures S3A and S3B). AcrIIA4 adopts

a fold composed of a triple-stranded  $\beta$  sheet with three  $\alpha$  helices positioned along one face of this  $\beta$  sheet (Figure S3C), with the electrostatics of its SpyCas9-interacting surface shown in Figure S3D. A DALI search detected no structural similarity between AcrIIA4 and reported structures, indicating that AcrIIA4 adopts an unidentified fold in the ternary complex.

The overall structure of SpyCas9 in the AcrIIA4-bound SpyCas9-sgRNA ternary complex is almost identical to that in the SpyCas9-sgRNA binary complex (Figure 2C). By contrast, addition of dsDNA to the SpyCas9-sgRNA binary complex



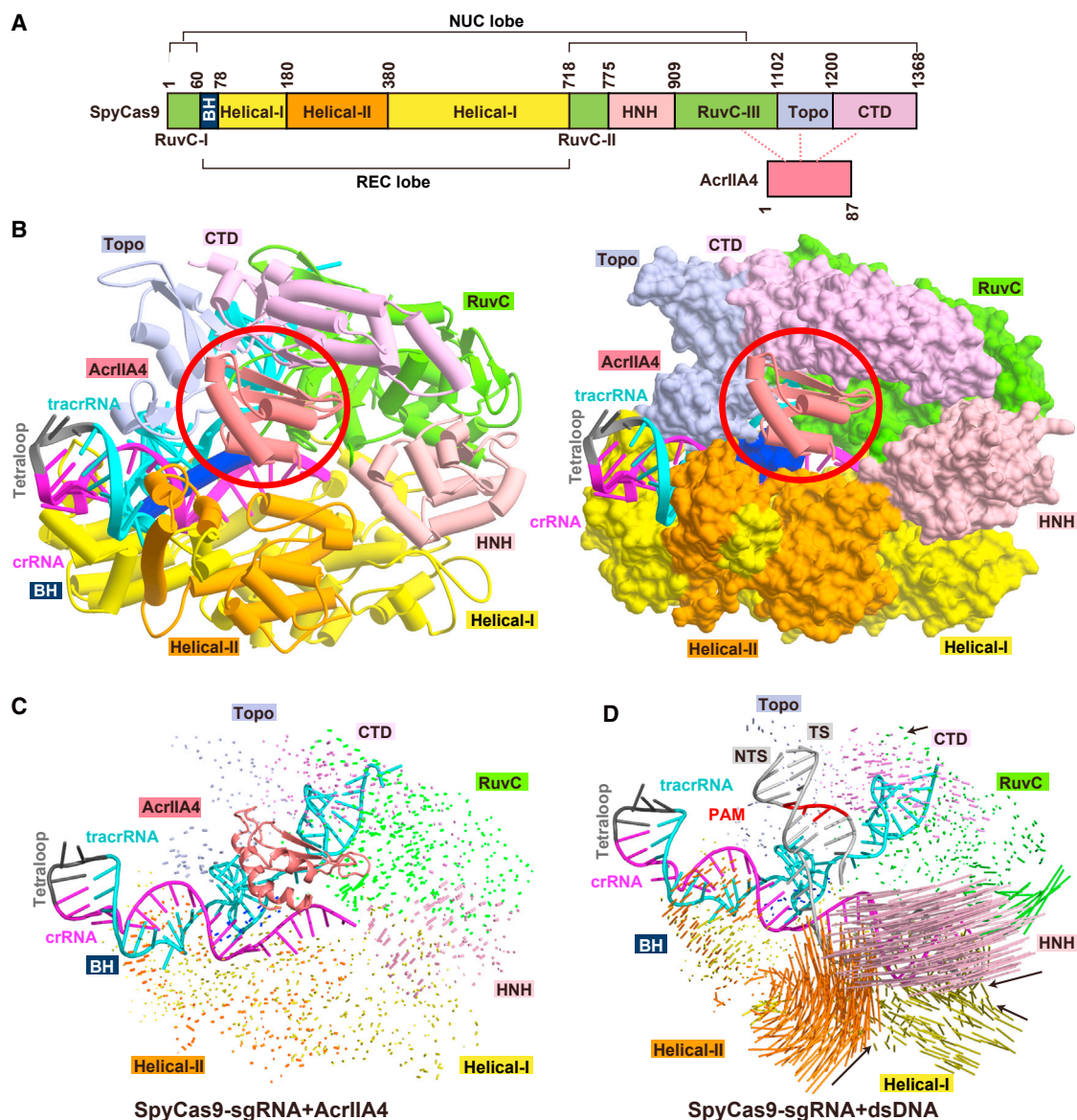


**Figure 2. Overall Structure of AcrIIA4-SpyCas9-sgRNA Complex**

(A) Domain organization of SpyCas9 and AcrIIA4.

(B) Ribbon and surface representations of AcrIIA4-SpyCas9-sgRNA ternary complex, color coded as defined in (A). The AcrIIA4 molecule in each view is highlighted by a red circle.

(C and D) Structural comparison of domain movement on proceeding from the SpyCas9-sgRNA binary complex to the SpyCas9-sgRNA-AcrIIA4 ternary complex (C) and to the SpyCas9-sgRNA-dsDNA ternary complex (D). Vector lengths correlate with the domain motion scales. TS and NTS represent target and non-target DNA strands, respectively.

See also Figures S2 and S4.

results in large conformational changes in the Helical and HNH domains of SpyCas9 (Figure 2D). These results establish that binding of AcrIIA4, in contrast to binding of dsDNA, induces minimal conformational changes of SpyCas9 within the SpyCas9-sgRNA context.

#### Recognition of sgRNA-Bound SpyCas9 by AcrIIA4

AcrIIA4 interacts with a positively charged surface of SpyCas9 formed by the Topo, RuvC, and CTD domains (Figure S3B) via

extensive hydrophilic contacts. The contacts with the Topo domain involve the  $\alpha$ 1- $\beta$ 1 loop (connecting helix  $\alpha$ 1 and  $\beta$  strand  $\beta$ 1) and  $\beta$ 2- $\beta$ 3 loop of bound AcrIIA4 (Figures 3A and 3B). The side chains of Asp14 and Asn36 of bound AcrIIA4 are involved in a hydrogen-bonding network with the main chains of Glu1108, Ser1109, and Ser1136, as well as the side chain of Ser1109 of the Topo domain (Figure 3B). It should be noted that the same Glu1108 and Ser1109 are key residues that stabilize the +1 phosphate, while key residue Ser1136 contacts the

**Table 1. Summary of Diffraction Data and Structure Refinement Statistics**

Data Collection	
Beam line	APS-ID24E
Wavelength (Å)	0.9792
Space group	P2 <sub>1</sub> 2 <sub>1</sub>
Cell parameters	
a, b, c (Å)	72.19, 101.24, 303.56
Resolution (Å)	50.0–2.60 (2.69–2.60) <sup>a</sup>
R <sub>merge</sub> (%)	9.2 (49.7)
Average I/σ(I)	14.3 (1.6)
Completeness (%)	94.6 (72.1)
CC (1/2)	0.805
Average redundancy	4.3 (3.4)
No. of unique reflections	65,587
Refinement	
R <sub>work</sub> /R <sub>free</sub> (%)	17.8/22.6
No. of non-H atoms	13,175
Average B factor (Å <sup>2</sup> )	
SpyCas9	60.1
AcrIIA4	53.6
RNA	60.6
RMS deviations	
Bond lengths (Å)	1.053
Bond angles (°)	0.009
Ramachandran plot (%)	
Favored	95.3
Allowed	4.7
Outliers	0

Related to Figures 1, 2, 3, and 4.

<sup>a</sup>Highest resolution shell (in Å) shown in parentheses.

base of a PAM nucleotide in the non-target DNA strand via a water molecule in the structure of the corresponding SpyCas9-sgRNA-dsDNA ternary complex (Anders et al., 2014).

The interface between AcrIIA4 (through its β2-β3 and α2-α3 loops) and the CTD domain consists of several hydrophilic interactions (Figures 3C and 3D). Residues Asp37 to Glu40 in the β2-β3 loop and the following β strand (β3) of bound AcrIIA4 interact with residues Lys1200, Ala1215, Ser1216, and Gln1221 in the CTD domain. It is worth noting that these residues in the CTD domain interact with the backbones of the PAM duplex in the structure of the corresponding SpyCas9-sgRNA-dsDNA ternary complex (Anders et al., 2014). Interestingly, residues Arg1333 and Arg1335 in the β-hairpin of the CTD domain, which are essential for the recognition of PAM sequence in the SpyCas9-sgRNA-dsDNA ternary complex (Anders et al., 2014), are instead recognized by residues Tyr67, Asp69, and Glu70 in the α2-α3 loop and residue Asn39 in β3 of bound AcrIIA4 (Figure 3D).

At the interface with the RuvC domain, an extensive intermolecular hydrogen bond network is formed involving Lys18 in β1 and Ser20 to Ser26 in the β1-β2 loop of AcrIIA4 (Figures 3E and 3F). Remarkably, the protruding β1-β2 loop of AcrIIA4 in-

serts into the active site of RuvC domain and hydrogen bonds with key residues (Glu762 and His 983) lining the RuvC catalytic pocket (Figure 3F). We used dSpyCas9 (D10A/H840A) for crystallization, so we modeled the side chain of Asp10 in the catalytic pocket based on reported structures (Anders et al., 2014; Jiang et al., 2015, 2016; Jinek et al., 2014; Nishimasu et al., 2014) and found that the side chain of key catalytic residue Asp10 could potentially hydrogen bond with Asn25 in the β1-β2 loop of bound AcrIIA4. These interactions between AcrIIA4 and key residues (Asp10, Glu762, and His983) lining the RuvC catalytic pocket result in the shielding of the active site and abolishing the access of non-target DNA strand into the active site.

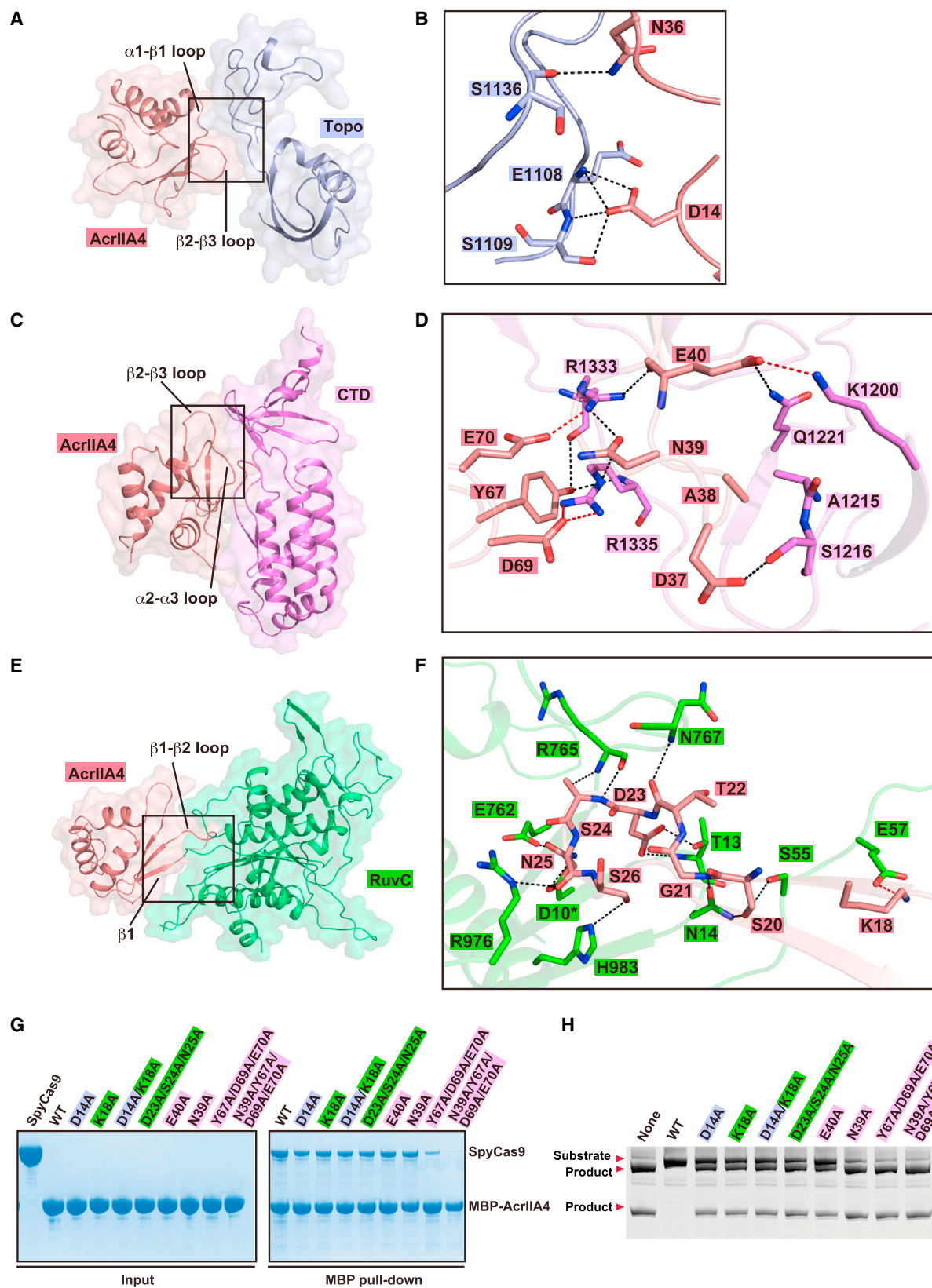
We generated single or multiple Ala mutations of AcrIIA4 residues involved in intermolecular contacts and investigated the impact of these mutations on binding to SpyCas9 and inhibition of catalytic activity. These AcrIIA4 Ala mutants show reduced binding affinity to SpyCas9, with the triple mutant Y67A/D69A/E70A and its tetra mutant counterpart containing also N39A, resulting in essentially complete loss in binding affinity (Figure 3G). Notably, in the related MBP pull-down assay, the same Ala mutants show reduced or complete loss in the inhibition capacity as monitored by cleavage of linear dsDNA (Figure 3H). Due to the extended hydrophilic intermolecular interactions at the interface between AcrIIA4 and SpyCas9, single alanine mutations at these sites show a relatively reduced impact (Figures 3G and 3H) when compared to single charge reversal mutations (Figures S3E and S3F). In addition, double or multiple alanine mutations at the interface (Figures 3G and 3H) show comparable impact to those observed for single charge reversal mutations (Figures S3E and S3F) (see also Dong et al., 2017).

### Competitive Binding by AcrIIA4 for PAM Duplex-Interacting Surface

AcrIIA4 targets the concave surface formed by the Topo, CTD, and RuvC domains in the SpyCas9-sgRNA binary complex and buries an area of 1,693 Å<sup>2</sup> on ternary complex formation (Figure 4A). By contrast, positioning of the PAM duplex of dsDNA on the surface formed by Topo and CTD domains of the SpyCas9-sgRNA binary complex buries an area of 553 Å<sup>2</sup> on ternary complex formation (Figure 4B). These results are indicative of AcrIIA4 having higher binding affinity than dsDNA for sgRNA-bound SpyCas9 binary complex. We investigated the extent to which AcrIIA4 and target dsDNA could competitively bind to the binary complex by electrophoretic mobility shift assays (EMSAs). Indeed, when supplied with AcrIIA4 and target dsDNA simultaneously, AcrIIA4 competed with dsDNA target to preferentially bind to the dSpyCas9-sgRNA binary complex (Figure 4C, left panel).

### AcrIIA4 Cannot Replace Bound dsDNA in Its Preformed Ternary Complex

On addition of AcrIIA4 to the preformed dSpyCas9-sgRNA-dsDNA ternary complex, no release of free DNA band was observed in EMSAs (Figure 4C, right panel), suggesting that AcrIIA4 cannot access and replace the bound dsDNA substrate. We also investigated whether AcrIIA2 shows the same behavior as AcrIIA4 and found that AcrIIA2 is also able to compete with dsDNA target for binding to dSpyCas9-sgRNA binary complex



(legend on next page)



but unable to release bound dsDNA from its preformed ternary complex (Figure S4A).

## DISCUSSION

### Blockage of PAM Duplex Recognition Interface by Bound AcrIIA4

The interface between AcrIIA4 and the Topo and CTD domains (Figure 4A) almost overlaps with that reported previously between dsDNA and these two domains (Figure 4B). Residues Asp37 to Glu40 in the  $\beta$ 2- $\beta$ 3 loop and Asp69 to Glu70 in the  $\alpha$ 2- $\alpha$ 3 loop of bound AcrIIA4 (Figure 4D; Figure S4B) occupy similar positions to those of the backbones of the PAM duplex (Figure 4E; Figure S4B) and form extensive interactions with residues associated with PAM duplex binding (Figures 4D and 4E).

Asp14 of the  $\alpha$ 1- $\beta$ 1 loop of AcrIIA4 (Figure 4D; Figure S4B) is positioned at the corresponding position occupied by the +1 phosphate group of target dsDNA (Figure 4E; Figure S4B) and interacts with Glu1108 and Ser1109 in the phosphate lock loop (Figure 4E). Separation of the double strands of target dsDNA and zipping up of the guide:target heteroduplex has been observed to start from the first nucleotide of the target DNA strand, with stabilization of +1 phosphate group important for kink formation in the target DNA strand at the junction between the PAM and guide-target duplexes (Anders et al., 2014). Hence, occupation of the phosphate lock site by bound AcrIIA4 would perturb formation of the guide:target heteroduplex. Moreover, Arg1333 and Arg1335 in the CTD domain that are critical for readout of the 5'-NGG PAM sequence (Figure 4E; Figure S4B) are recognized by AcrIIA4 (Figure 4D; Figure S4B), resulting in inhibition of readout of the PAM sequence.

Taken together, the relatively larger and overlapped interface ensures that AcrIIA4 could competitively interact with and occupy the PAM duplex-interaction surface, thereby blocking the binding of dsDNA substrate. In summary, AcrIIA4 “locks” and “covers” all the key residues involved in PAM duplex and +1 phosphate group recognition.

### Blockage of RuvC Active Site by AcrIIA4

At the interface with the RuvC domain, the protruding  $\beta$ 1- $\beta$ 2 loop and  $\beta$ 1 of AcrIIA4 are directed toward the active site within the RuvC domain, as well as the tunnel for entrance of the non-target strand into RuvC active site (Figures 4A and 4B; Figure S4B). Ser20 to Ser26 of the  $\beta$ 1- $\beta$ 2 loop and Lys18 of  $\beta$ 1 of AcrIIA4 form contacts with residues within and adjacent to the active site (Figure 3F), especially key catalytic residues Glu762, His983, and the modeled side chain of Asp10 (Figures 4F and 4G), thereby preventing the entrance of non-target DNA strand into the active site of the RuvC domain.

### Selective Binding of AcrIIA4 to sgRNA-Bound SpyCas9

During the transition from the apo state to the pre-target sgRNA-bound binary complex, the REC lobe undergoes large conformational changes, while small conformational changes are observed for the NUC lobe (Figure S4C) (Jinek et al., 2014; Jiang et al., 2015). In addition, several regions in the NUC lobe become ordered upon sgRNA binding. Some of these regions in the binary complex are targeted by AcrIIA4 on ternary complex formation. Specifically, the Gly1103 to Ser1136 segment of the Topo domain undergoes a disordered-to-ordered transition on binary complex formation, thereby defining a surface targeted by the  $\alpha$ 1- $\beta$ 1 and  $\beta$ 2- $\beta$ 3 loops of bound AcrIIA4 (Figure 3B). The Arg765 to Gln774 segment connecting RuvC and HNH domains is also disordered in the apo state and becomes ordered on binary complex formation, such that the backbone of Arg765 and Asn767 forms hydrogen bonds with the  $\beta$ 1- $\beta$ 2 loop of bound AcrIIA4 (Figure 3F). The movements of Helical-I on proceeding from apo to sgRNA-bound states also alters the orientation of the loop (Ser55 to Glu60) between BH and RuvC-I domains, which results in the formation of hydrogen contacts between sgRNA-bound SpyCas9 and bound AcrIIA4 (Figure 3F). In addition, small movements of the CTD domain on binary complex formation may also provide a better shape-complementary surface for AcrIIA4. These structural results provide a possible explanation why AcrIIA4 has higher binding affinity to sgRNA-bound SpyCas9 than apo-SpyCas9 and as a result selectively recognizes the SpyCas9 binary complex.

Upon dsDNA binding to form the ternary complex, the Helical-I and Helical-II domains of the REC lobe undergo further domain movements, as does the HNH domain of the NUC lobe (Figure 2D) (Anders et al., 2014; Jiang et al., 2015, 2016; Nishimasu et al., 2014). The HNH domain moves toward the target strand cleavage site that is adjacent to the PAM duplex, thereby resulting in the formation of a narrow channel, which limits access by AcrIIA4 and its replacement of bound dsDNA. This appears to explain why AcrIIA4 shows either extremely weak or no binding to the SpyCas9-sgRNA-DNA ternary complex (Figures 1B and 1C).

It should be noted that blockage of dsDNA binding is distinct from inhibition of nuclease activity, given that our current understanding of Cas9 cleavage mechanism is that its nuclease activity is only activated upon proper DNA target recognition and R-loop formation (Sternberg et al., 2014, 2015).

### Comparison of Anti-CRISPR Proteins Targeting Cas9 versus Cascade Complexes

To date, there are three reported structures of anti-CRISPR proteins, including AcrF3 that targets *P. aeruginosa* type I-F Cas3

### Figure 3. Detailed Interactions of AcrIIA4 with sgRNA-Bound SpyCas9

(A, C, and E) Surface views of the interfaces between AcrIIA4 and Topo domain (A), CTD domain (C), and RuvC domain (E). The interface segments are highlighted by black boxes.

(B, D, and F) Detailed interactions at the interfaces between AcrIIA4 and Topo domain (B), CTD domain (D), and RuvC domain (F) are shown in stick representations. The color code is the same as Figure 2A. Hydrogen bonds and salt bridges are colored as black and red dashed lines, respectively.

(G) Mutation analysis of AcrIIA4 residues involved in the binding to sgRNA-bound SpyCas9 by MBP pull-down assay of MBP-tagged AcrIIA4.

(H) In vitro enzymatic assay of Ala mutations of AcrIIA4 residues that impaired or abolished binding of AcrIIA4 to sgRNA-bound SpyCas9.

See also Figure S3.



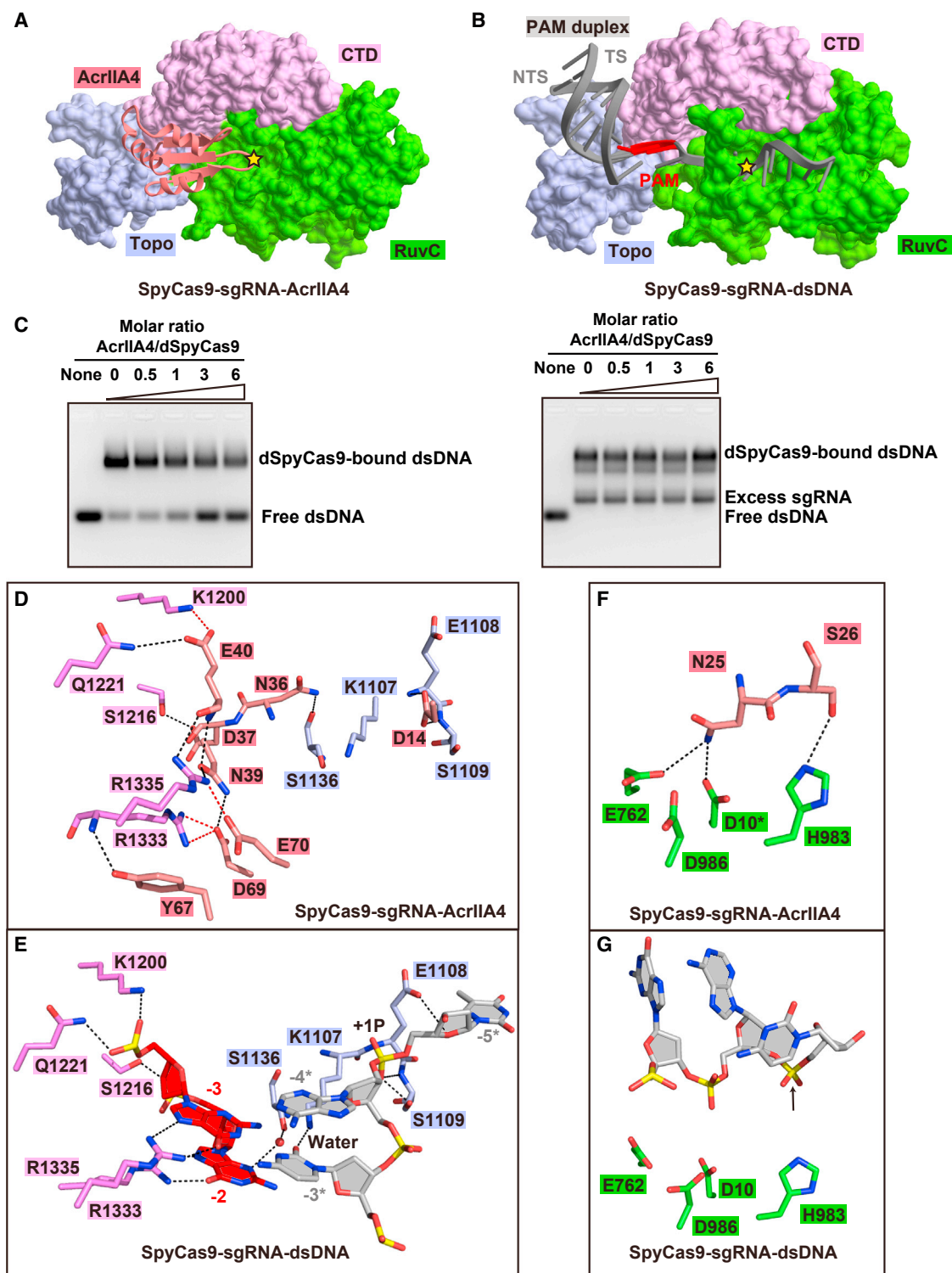


**Figure 4. Inhibition Mechanism of SpyCas9 by AcrIIA4**

(A and B) Recognition of AcrIIA4 (A) and the PAM duplex (B) by Topo, CTD, and RuvC domains of SpyCas9. The active site of RuvC domain for non-target DNA strand in each panel is highlighted by a yellow star. TS and NTS represent target and non-target DNA strands, respectively. (C) AcrIIA4 competitively binding to preformed SpyCas9-sgRNA binary complex (left) rather than SpyCas9-sgRNA-dsDNA ternary complex (right) in EMSA assays. The molar ratios of AcrIIA4:SpyCas9 are shown at the top of the gel.

(legend continued on next page)

(Wang et al., 2016b; Wang et al., 2016c) and AcrF1 and AcrF2 that target *P. aeruginosa* type I-F Csy cascade (Chowdhury et al., 2017). All these inhibitors, as well as AcrIIA4, share low sequence identity and adopt divergent overall structures (Figure S3C and S4D–S4F, upper panels). AcrF1, AcrF2, and AcrIIA4 are composed of one variant  $\beta$  sheet and several  $\alpha$  helices, whereas AcrF3 is composed of six  $\alpha$  helices. In addition, these inhibitors employ distinct inhibition mechanisms, with AcrF1 and AcrF2 targeting distinct sites on Csy cascade. AcrF2 contacts the PAM-interacting region of Csy cascade through its negatively charged surface (Figures S3D and S4D, lower panel), while AcrF1 blocks the hybridization of target DNA strand with crRNA. AcrF3 functions as a dimer and prevents target DNA access to its binding site, as well as prevents recognition of Cas3 by upstream Cascade, and activation by ATP. AcrIIA4, like AcrF2, prevents PAM duplex access to its binding site and also blocks non-target DNA strand access to the RuvC catalytic pocket. However, no common interaction model could be formulated involving these four inhibitors, suggesting that divergent anti-CRISPR proteins are likely to have evolved independently, thereby targeting variant CRISPR-Cas systems.

## Summary

Anti-CRISPR AcrIIA4 protein antagonizes the CRISPR-Cas9 host-defense system through abolishment of all possible contributors governing the activity of SpyCas9, which includes prohibiting the recognition and access of the PAM duplex, blocking the tunnel for non-target DNA strand access, and through occupancy of the catalytic pocket in the RuvC domain. In addition, AcrIIA4 exhibits higher binding affinity than dsDNA for sgRNA-bound SpyCas9 and is able to competitively bind to the binary complex, resulting in the inactivation of SpyCas9. AcrIIA4 specifically binds to sgRNA-bound SpyCas9 rather than either apo or dsDNA-bound SpyCas9-sgRNA ternary complex, indicative of high efficiency for the inhibition. The pre-target sgRNA-bound state is ready for loading and cleavage of dsDNA target; however, apo-SpyCas9 requires either sgRNA or crRNA/tracrRNA binding in order to achieve the conformational changes needed for dsDNA target loading. For the dsDNA target-bound SpyCas9-sgRNA ternary complex, displacement of the PAM duplex or melting of the guide: target heteroduplex requires overcoming a high energy barrier. In addition, domain rearrangement during pre-target-bound to target-dsDNA-bound generates a narrow surface for optimal recognition of the PAM duplex, which is not suitable for AcrIIA4 association.

During preparation of our manuscript for submission, a related paper has appeared online in Nature outlining structural studies of AcrIIA4 bound to sgRNA-bound SpyCas9 (Dong et al., 2017), with this study and our contribution reaching common conclusions on anti-CRISPR mediated targeting of the cleavage activity of Cas9 endonucleases.

## STAR★METHODS

Detailed methods are provided in the online version of this paper and include the following:

- KEY RESOURCES TABLE
- CONTACT FOR REAGENT AND RESOURCE SHARING
- EXPERIMENTAL MODEL AND SUBJECT DETAILS
- METHOD DETAILS
  - Protein Expression and Purification
  - Crystallization, Data Collection, and Structure Determination
  - In Vitro Transcription and Purification of sgRNA
  - In Vitro Cleavage Assay
  - SEC-MALLS
  - Size-Exclusion Chromatography Assay
  - MBP Pull-Down Assay
  - Electrophoretic Mobility Shift Assay (EMSA)
- QUANTIFICATION AND STATISTICAL ANALYSIS
- DATA AND SOFTWARE AVAILABILITY

## SUPPLEMENTAL INFORMATION

Supplemental Information includes four figures and can be found with this article online at <http://dx.doi.org/10.1016/j.molcel.2017.05.024>.

## AUTHOR CONTRIBUTIONS

H.Y. undertook all the biochemical and structural studies under the supervision of D.J.P.

## ACKNOWLEDGMENTS

X-ray diffraction studies were conducted at the Advanced Photon Source on the Northeastern Collaborative Access Team beamlines, which are supported by NIGMS grant P41GM103403 and U.S. Department of Energy grant DE-AC02-06CH11357. The Pilatus 6M detector on 24-ID-C beam line is funded by a NIHORIP HEI grant (S10 RR029205). The research was supported by NIH grant GM104962 to D.J.P. and by the Memorial Sloan Kettering Cancer Center Core Grant (P30CA008748).

Received: May 7, 2017

Revised: May 19, 2017

Accepted: May 22, 2017

Published: June 8, 2017

## REFERENCES

- Abudayyeh, O.O., Gootenberg, J.S., Konermann, S., Joung, J., Slaymaker, I.M., Cox, D.B., Shmakov, S., Makarova, K.S., Semenova, E., Minakhin, L., et al. (2016). C2c2 is a single-component programmable RNA-guided RNA-targeting CRISPR effector. *Science* 353, aaf5573.
- Adams, P.D., Grosse-Kunstleve, R.W., Hung, L.W., Ioerger, T.R., McCoy, A.J., Moriarty, N.W., Read, R.J., Sacchettini, J.C., Sauter, N.K., and Terwilliger, T.C. (2002). PHENIX: building new software for automated crystallographic structure determination. *Acta Crystallogr. D Biol. Crystallogr.* 58, 1948–1954.

(D and E) Detailed interactions between AcrIIA4 (D) and PAM duplex (E) with the Topo and CTD domains of SpyCas9, respectively.

(F and G) Recognition of key catalytic residues in the RuvC active site by AcrIIA4 (F) and non-target DNA strand (G). The modeled side chain of catalytic residue Asp10 is marked by asterisk. The position of cleavage site in non-target DNA strand is pointed by a black arrow.

See also Figure S4.

- Anders, C., Niewoehner, O., Duerst, A., and Jinek, M. (2014). Structural basis of PAM-dependent target DNA recognition by the Cas9 endonuclease. *Nature* 513, 569–573.
- Barrangou, R., and Doudna, J.A. (2016). Applications of CRISPR technologies in research and beyond. *Nat. Biotechnol.* 34, 933–941.
- Barrangou, R., Fremaux, C., Deveau, H., Richards, M., Boyaval, P., Moineau, S., Romero, D.A., and Horvath, P. (2007). CRISPR provides acquired resistance against viruses in prokaryotes. *Science* 315, 1709–1712.
- Bondy-Denomy, J., Pawluk, A., Maxwell, K.L., and Davidson, A.R. (2013). Bacteriophage genes that inactivate the CRISPR/Cas bacterial immune system. *Nature* 493, 429–432.
- Bondy-Denomy, J., Garcia, B., Strum, S., Du, M., Rollins, M.F., Hidalgo-Reyes, Y., Wiedenheft, B., Maxwell, K.L., and Davidson, A.R. (2015). Multiple mechanisms for CRISPR-Cas inhibition by anti-CRISPR proteins. *Nature* 526, 136–139.
- Chowdhury, S., Carter, J., Rollins, M.F., Golden, S.M., Jackson, R.N., Hoffmann, C., Nosaka, L., Bondy-Denomy, J., Maxwell, K.L., Davidson, A.R., et al. (2017). Structure reveals mechanisms of viral suppressors that intercept a CRISPR RNA-guided surveillance complex. *Cell* 169, 47–57.e11.
- Deltcheva, E., Chylinski, K., Sharma, C.M., Gonzales, K., Chao, Y., Pirzada, Z.A., Eckert, M.R., Vogel, J., and Charpentier, E. (2011). CRISPR RNA maturation by trans-encoded small RNA and host factor RNase III. *Nature* 471, 602–607.
- Deveau, H., Barrangou, R., Garneau, J.E., Labonté, J., Fremaux, C., Boyaval, P., Romero, D.A., Horvath, P., and Moineau, S. (2008). Phage response to CRISPR-encoded resistance in *Streptococcus thermophilus*. *J. Bacteriol.* 190, 1390–1400.
- Dominguez, A.A., Lim, W.A., and Qi, L.S. (2016). Beyond editing: repurposing CRISPR-Cas9 for precision genome regulation and interrogation. *Nat. Rev. Mol. Cell Biol.* 17, 5–15.
- Dong, D., Guo, M., Wang, S., Zhu, Y., Wang, S., Xiong, Z., Yang, J., Xu, Z., and Huang, Z. (2017). Structural basis of CRISPR-SpyCas9 inhibition by an anti-CRISPR protein. *Nature*. Published online April 27, 2017. <http://dx.doi.org/10.1038/nature22377>.
- Dupuis, M.E., Villion, M., Magadán, A.H., and Moineau, S. (2013). CRISPR-Cas and restriction-modification systems are compatible and increase phage resistance. *Nat. Commun.* 4, 2087.
- East-Seletsky, A., O'Connell, M.R., Knight, S.C., Burstein, D., Cate, J.H., Tjian, R., and Doudna, J.A. (2016). Two distinct RNase activities of CRISPR-C2c2 enable guide-RNA processing and RNA detection. *Nature* 538, 270–273.
- East-Seletsky, A., O'Connell, M.R., Burstein, D., Knott, G.J., and Doudna, J.A. (2017). RNA targeting by functionally orthogonal type VI-A CRISPR-Cas enzymes. *Mol. Cell* 66, 373–383.e3.
- Emsley, P., Lohkamp, B., Scott, W.G., and Cowtan, K. (2010). Features and development of Coot. *Acta Crystallogr. D Biol. Crystallogr.* 66, 486–501.
- Garneau, J.E., Dupuis, M.E., Villion, M., Romero, D.A., Barrangou, R., Boyaval, P., Fremaux, C., Horvath, P., Magadán, A.H., and Moineau, S. (2010). The CRISPR/Cas bacterial immune system cleaves bacteriophage and plasmid DNA. *Nature* 468, 67–71.
- Gasiunas, G., Barrangou, R., Horvath, P., and Siksnys, V. (2012). Cas9-crRNA ribonucleoprotein complex mediates specific DNA cleavage for adaptive immunity in bacteria. *Proc. Natl. Acad. Sci. USA* 109, E2579–E2586.
- Gootenberg, J.S., Abudayyeh, O.O., Lee, J.W., Essletzbichler, P., Dy, A.J., Joung, J., Verdine, V., Donghia, N., Daringer, N.M., Freije, C.A., et al. (2017). Nucleic acid detection with CRISPR-Cas13a/C2c2. *Science* 356, 438–442.
- Hille, F., and Charpentier, E. (2016). CRISPR-Cas: biology, mechanisms and relevance. *Philos. Trans. R. Soc. Lond. B Biol. Sci.* 371, 371.
- Hsu, P.D., Lander, E.S., and Zhang, F. (2014). Development and applications of CRISPR-Cas9 for genome engineering. *Cell* 157, 1262–1278.
- Jiang, W., and Marraffini, L.A. (2015). CRISPR-Cas: new tools for genetic manipulations from bacterial immunity systems. *Annu. Rev. Microbiol.* 69, 209–228.
- Jiang, F., Zhou, K., Ma, L., Gressel, S., and Doudna, J.A. (2015). STRUCTURAL BIOLOGY. A Cas9-guide RNA complex preorganized for target DNA recognition. *Science* 348, 1477–1481.
- Jiang, F., Taylor, D.W., Chen, J.S., Kornfeld, J.E., Zhou, K., Thompson, A.J., Nogales, E., and Doudna, J.A. (2016). Structures of a CRISPR-Cas9 R-loop complex primed for DNA cleavage. *Science* 351, 867–871.
- Jinek, M., Chylinski, K., Fonfara, I., Hauer, M., Doudna, J.A., and Charpentier, E. (2012). A programmable dual-RNA-guided DNA endonuclease in adaptive bacterial immunity. *Science* 337, 816–821.
- Jinek, M., Jiang, F., Taylor, D.W., Sternberg, S.H., Kaya, E., Ma, E., Anders, C., Hauer, M., Zhou, K., Lin, S., et al. (2014). Structures of Cas9 endonucleases reveal RNA-mediated conformational activation. *Science* 343, 1247997.
- Labrie, S.J., Samson, J.E., and Moineau, S. (2010). Bacteriophage resistance mechanisms. *Nat. Rev. Microbiol.* 8, 317–327.
- Liu, L., Li, X., Wang, J., Wang, M., Chen, P., Yin, M., Li, J., Sheng, G., and Wang, Y. (2017). Two distant catalytic sites are responsible for C2c2 RNase activities. *Cell* 168, 121–134.e12.
- Makarova, K.S., Haft, D.H., Barrangou, R., Brouns, S.J., Charpentier, E., Horvath, P., Moineau, S., Mojica, F.J., Wolf, Y.I., Yakunin, A.F., et al. (2011). Evolution and classification of the CRISPR-Cas systems. *Nat. Rev. Microbiol.* 9, 467–477.
- Makarova, K.S., Wolf, Y.I., Alkhnbashi, O.S., Costa, F., Shah, S.A., Saunders, S.J., Barrangou, R., Brouns, S.J., Charpentier, E., Haft, D.H., et al. (2015). An updated evolutionary classification of CRISPR-Cas systems. *Nat. Rev. Microbiol.* 13, 722–736.
- Marraffini, L.A. (2015). CRISPR-Cas immunity in prokaryotes. *Nature* 526, 55–61.
- Mohanraju, P., Makarova, K.S., Zetsche, B., Zhang, F., Koonin, E.V., and van der Oost, J. (2016). Diverse evolutionary roots and mechanistic variations of the CRISPR-Cas systems. *Science* 353, aad5147.
- Mojica, F.J., Díez-Villasenor, C., García-Martínez, J., and Almendros, C. (2009). Short motif sequences determine the targets of the prokaryotic CRISPR defence system. *Microbiology* 155, 733–740.
- Nishimasu, H., and Nureki, O. (2017). Structures and mechanisms of CRISPR RNA-guided effector nucleases. *Curr. Opin. Struct. Biol.* 43, 68–78.
- Nishimasu, H., Ran, F.A., Hsu, P.D., Konermann, S., Shehata, S.I., Dohmae, N., Ishitani, R., Zhang, F., and Nureki, O. (2014). Crystal structure of Cas9 in complex with guide RNA and target DNA. *Cell* 156, 935–949.
- Otwinowski, Z., and Minor, W. (1997). Processing of X-ray diffraction data collected in oscillation mode. *Methods Enzymol.* 276, 307–326.
- Pawluk, A., Bondy-Denomy, J., Cheung, V.H., Maxwell, K.L., and Davidson, A.R. (2014). A new group of phage anti-CRISPR genes inhibits the type I-E CRISPR-Cas system of *Pseudomonas aeruginosa*. *MBio* 5, e00896.
- Pawluk, A., Amrani, N., Zhang, Y., Garcia, B., Hidalgo-Reyes, Y., Lee, J., Edraki, A., Shah, M., Sontheimer, E.J., Maxwell, K.L., and Davidson, A.R. (2016a). Naturally occurring off-switches for CRISPR-Cas9. *Cell* 167, 1829–1838.e9.
- Pawluk, A., Staals, R.H., Taylor, C., Watson, B.N., Saha, S., Fineran, P.C., Maxwell, K.L., and Davidson, A.R. (2016b). Inactivation of CRISPR-Cas systems by anti-CRISPR proteins in diverse bacterial species. *Nat. Microbiol.* 1, 16085.
- Qi, L.S., Larson, M.H., Gilbert, L.A., Doudna, J.A., Weissman, J.S., Arkin, A.P., and Lim, W.A. (2013). Repurposing CRISPR as an RNA-guided platform for sequence-specific control of gene expression. *Cell* 152, 1173–1183.
- Rauch, B.J., Silvis, M.R., Hultquist, J.F., Waters, C.S., McGregor, M.J., Krogan, N.J., and Bondy-Denomy, J. (2017). Inhibition of CRISPR-Cas9 with bacteriophage proteins. *Cell* 168, 150–158.e10.
- Samson, J.E., Magadán, A.H., Sabri, M., and Moineau, S. (2013). Revenge of the phages: defeating bacterial defences. *Nat. Rev. Microbiol.* 11, 675–687.

- Shmakov, S., Abudayyeh, O.O., Makarova, K.S., Wolf, Y.I., Gootenberg, J.S., Semenova, E., Minakhin, L., Joung, J., Konermann, S., Severinov, K., et al. (2015). Discovery and functional characterization of diverse class 2 CRISPR-Cas systems. *Mol. Cell* 60, 385–397.
- Smargon, A.A., Cox, D.B., Pyzocha, N.K., Zheng, K., Slaymaker, I.M., Gootenberg, J.S., Abudayyeh, O.A., Essletzbichler, P., Shmakov, S., Makarova, K.S., et al. (2017). Cas13b is a type VI-B CRISPR-associated RNA-guided RNase differentially regulated by accessory proteins Csx27 and Csx28. *Mol. Cell* 65, 618–630.e7.
- Sternberg, S.H., and Doudna, J.A. (2015). Expanding the biologist's toolkit with CRISPR-Cas9. *Mol. Cell* 58, 568–574.
- Sternberg, S.H., Redding, S., Jinek, M., Greene, E.C., and Doudna, J.A. (2014). DNA interrogation by the CRISPR RNA-guided endonuclease Cas9. *Nature* 507, 62–67.
- Sternberg, S.H., LaFrance, B., Kaplan, M., and Doudna, J.A. (2015). Conformational control of DNA target cleavage by CRISPR-Cas9. *Nature* 527, 110–113.
- van der Oost, J., Jore, M.M., Westra, E.R., Lundgren, M., and Brouns, S.J. (2009). CRISPR-based adaptive and heritable immunity in prokaryotes. *Trends Biochem. Sci.* 34, 401–407.
- Wang, H., La Russa, M., and Qi, L.S. (2016a). CRISPR/Cas9 in genome editing and beyond. *Annu. Rev. Biochem.* 85, 227–264.
- Wang, J., Ma, J., Cheng, Z., Meng, X., You, L., Wang, M., Zhang, X., and Wang, Y. (2016b). A CRISPR evolutionary arms race: structural insights into viral anti-CRISPR/Cas responses. *Cell Res.* 26, 1165–1168.
- Wang, X., Yao, D., Xu, J.G., Li, A.R., Xu, J., Fu, P., Zhou, Y., and Zhu, Y. (2016c). Structural basis of Cas3 inhibition by the bacteriophage protein AcrF3. *Nat. Struct. Mol. Biol.* 23, 868–870.
- Wright, A.V., Nuñez, J.K., and Doudna, J.A. (2016). Biology and applications of CRISPR systems: harnessing nature's toolbox for genome engineering. *Cell* 164, 29–44.
- Zetsche, B., Gootenberg, J.S., Abudayyeh, O.O., Slaymaker, I.M., Makarova, K.S., Essletzbichler, P., Volz, S.E., Joung, J., van der Oost, J., Regev, A., et al. (2015). Cpf1 is a single RNA-guided endonuclease of a class 2 CRISPR-Cas system. *Cell* 163, 759–771.



## STAR★METHODS

## KEY RESOURCES TABLE

REAGENT or RESOURCE	SOURCE	IDENTIFIER
Chemicals, Peptides, and Recombinant Proteins		
ULP1	Homemade	N/A
T7 RNA polymerase	Homemade	N/A
1 M HEPES sodium salt, pH 7.0	QIAGEN	Cat#133254
50% w/v PEG 3350	QIAGEN	Cat#133083
Ethylene glycol	QIAGEN	Cat#133044
Urea	Sigma-Aldrich	CAS: 57-13-6 Cat#U5378-5KG
Diethyl pyrocarbonate	Sigma-Aldrich	CAS: 1609-47-8 Cat# D5758-50ML
40% acrylamide and bis-acrylamide solution, 29:1	Bio-Rad	Cat#161-0146
Critical Commercial Assays		
NeXtal Tubes Classics II Suite	QIAGEN	Cat#130723
High Pure PCR Product Purification Kit	Roche	Cat#11732676001
PureLink HiPure Plasmid Megaprep Kit	Thermo Fisher Scientific	Cat#K210008
Deposited Data		
SpyCas9-sgRNA-AcrIIA4 ternary complex structure	This paper	PDB: 5VW1
Raw image data	This paper	<a href="https://dx.doi.org/10.17632/34cnpysb7k.1">https://dx.doi.org/10.17632/34cnpysb7k.1</a>
Experimental Models: Organisms/Strains		
E.coli: BL21(DE3) Competent cells	Novagen	Cat#69450-3
E.coli: DH5 $\alpha$ Competent cells	Thermo Fisher Scientific	Cat#18265017
Recombinant DNA		
pRSF-Duet-1-His <sub>6</sub> -SUMO-SpyCas9	This paper	N/A
pRSF-Duet-1-His <sub>6</sub> -SUMO-SpyCas9-D10A/H840A	This paper	N/A
pMAL-His <sub>6</sub> -MBP-SpyCas9	This paper	N/A
pRSF-Duet-1-His <sub>6</sub> -SUMO-AcrIIA4	This paper	N/A
pRSF-Duet-1-His <sub>6</sub> -SUMO-AcrIIA4-D14A	This paper	N/A
pRSF-Duet-1-His <sub>6</sub> -SUMO-AcrIIA4-K18A	This paper	N/A
pRSF-Duet-1-His <sub>6</sub> -SUMO-AcrIIA4-D14A/K18A	This paper	N/A
pRSF-Duet-1-His <sub>6</sub> -SUMO-AcrIIA4-D23A/S24A/N25A	This paper	N/A
pRSF-Duet-1-His <sub>6</sub> -SUMO-AcrIIA4-N39A	This paper	N/A
pRSF-Duet-1-His <sub>6</sub> -SUMO-AcrIIA4-E40A	This paper	N/A
pRSF-Duet-1-His <sub>6</sub> -SUMO-AcrIIA4-Y67A/D69A/E70A	This paper	N/A
pRSF-Duet-1-His <sub>6</sub> -SUMO-AcrIIA4-N39A/Y67A/D69A/E70A	This paper	N/A
pMAL-His <sub>6</sub> -MBP-AcrIIA4	This paper	N/A
pMAL-His <sub>6</sub> -MBP-AcrIIA4-D14A	This paper	N/A
pMAL-His <sub>6</sub> -MBP-AcrIIA4-K18A	This paper	N/A
pMAL-His <sub>6</sub> -MBP-AcrIIA4-D14A/K18A	This paper	N/A
pMAL-His <sub>6</sub> -MBP-AcrIIA4-D23A/S24A/N25A	This paper	N/A
pMAL-His <sub>6</sub> -MBP-AcrIIA4-N39A	This paper	N/A
pMAL-His <sub>6</sub> -MBP-AcrIIA4-E40A	This paper	N/A
pMAL-His <sub>6</sub> -MBP-AcrIIA4-Y67A/D69A/E70A	This paper	N/A
pMAL-His <sub>6</sub> -MBP-AcrIIA4-N39A/Y67A/D69A/E70A	This paper	N/A
pRSF-Duet-1-His <sub>6</sub> -SUMO-AcrIIA4-D14K	This paper	N/A

(Continued on next page)

**Continued**

REAGENT or RESOURCE	SOURCE	IDENTIFIER
pRSF-Duet-1-His <sub>6</sub> -SUMO-AcrIIA4-K18D	This paper	N/A
pRSF-Duet-1-His <sub>6</sub> -SUMO-AcrIIA4-D23K	This paper	N/A
pRSF-Duet-1-His <sub>6</sub> -SUMO-AcrIIA4-N25K	This paper	N/A
pRSF-Duet-1-His <sub>6</sub> -SUMO-AcrIIA4-S26K	This paper	N/A
pRSF-Duet-1-His <sub>6</sub> -SUMO-AcrIIA4-N39K	This paper	N/A
pRSF-Duet-1-His <sub>6</sub> -SUMO-AcrIIA4-E40K	This paper	N/A
pRSF-Duet-1-His <sub>6</sub> -SUMO-AcrIIA4-Y67K	This paper	N/A
pRSF-Duet-1-His <sub>6</sub> -SUMO-AcrIIA4-D69K	This paper	N/A
pRSF-Duet-1-His <sub>6</sub> -SUMO-AcrIIA4-E70K	This paper	N/A
pMAL-His <sub>6</sub> -MBP-AcrIIA4-D14K	This paper	N/A
pMAL-His <sub>6</sub> -MBP-AcrIIA4-K18D	This paper	N/A
pMAL-His <sub>6</sub> -MBP-AcrIIA4-D23K	This paper	N/A
pMAL-His <sub>6</sub> -MBP-AcrIIA4-N25K	This paper	N/A
pMAL-His <sub>6</sub> -MBP-AcrIIA4-S26K	This paper	N/A
pMAL-His <sub>6</sub> -MBP-AcrIIA4-N39K	This paper	N/A
pMAL-His <sub>6</sub> -MBP-AcrIIA4-E40K	This paper	N/A
pMAL-His <sub>6</sub> -MBP-AcrIIA4-Y67K	This paper	N/A
pMAL-His <sub>6</sub> -MBP-AcrIIA4-D69K	This paper	N/A
pMAL-His <sub>6</sub> -MBP-AcrIIA4-E70K	This paper	N/A
pRSF-Duet-1-His <sub>6</sub> -SUMO-AcrIIA2	This paper	N/A
pUT7-sgRNA	This paper	N/A
Sequence-Based Reagents		
28-nt non-target DNA strand ATAACTCAATTTGTAAAAATGGTATTG	IDT	N/A
28-nt target DNA strand CAATACCATTTTTACAAATTGAGTTAT	IDT	N/A
Software and Algorithms		
Coot	Emsley et al., 2010	<a href="http://www2.mrc-lmb.cam.ac.uk/personal/pemsley/coot">http://www2.mrc-lmb.cam.ac.uk/personal/pemsley/coot</a>
Phenix	Adams et al., 2002	<a href="https://www.phenix-online.org">https://www.phenix-online.org</a>
HKL2000	Otwinowski and Minor, 1997	<a href="http://www.hkl-xray.com/">http://www.hkl-xray.com/</a>
PyMOL	The PyMOL Molecular Graphics System, Version 1.8.4.0, Schrodinger, LLC	<a href="http://www.pymol.org">http://www.pymol.org</a>
CueMol	Version 2.2.2.397	<a href="http://www.cuemol.org">http://www.cuemol.org</a>
Other		
Amicon concentrators (3K)	Millipore	Cat#UFC900324
Amicon concentrators (30K)	Millipore	Cat#UFC903024
Amylose resin	New England Biolabs	Cat#E8021L
HisTrap FF (5 mL)	GE Healthcare	Cat#17-5255-01
HiTrap Heparin HP (5 mL)	GE Healthcare	Cat#17-0407-03
HiTrap Q Sepharose FF (5 mL)	GE Healthcare	Cat#17-5156-01
HiLoad 16/600 Superdex 200 pg	GE Healthcare	Cat#28989335
Superdex 75 10/300 GL	GE Healthcare	Cat#17517401
Superdex 200 10/300 GL	GE Healthcare	Cat#17517501
10% TBE-Urea gels	Thermo Fisher Scientific	Cat#EC68752BOX
Whatman Elutrap electroelution system	Sigma-Aldrich	Cat#WHA10447700

## CONTACT FOR REAGENT AND RESOURCE SHARING

Further information and requests for reagents could be directed to, and will be fulfilled by Dinshaw Patel ([pateld@mskcc.org](mailto:pateld@mskcc.org)).

## EXPERIMENTAL MODEL AND SUBJECT DETAILS

Plasmid DNA for in vitro transcription was amplified in *Escherichia coli* DH5 $\alpha$  strain in Lysogeny broth (LB) medium at 37°C overnight.

Recombinant proteins were overexpressed in *Escherichia coli* BL21 (DE3) strain in Lysogeny broth (LB) medium. The cells were grown at 37°C until OD600 reached 0.8 and then induced with 0.25 mM isopropyl  $\beta$ -D-1-thiogalactopyranoside (GoldBio) at 18°C for 20 hr.

## METHOD DETAILS

### Protein Expression and Purification

The gene encoding full-length *Streptococcus pyogenes* cas9 was synthesized and inserted into a modified pRSF-Duet-1 vector (Novagen) with N-terminal His6-SUMO tag following an ubiquitin-like protease (ULP1) cleavage site. Recombinant protein was overexpressed in *Escherichia coli* BL21 (DE3) strain in Lysogeny broth (LB) medium. The cells were grown at 37°C until OD600 reached 0.8 and then induced with 0.25 mM isopropyl  $\beta$ -D-1-thiogalactopyranoside (GoldBio) at 18°C for 20 hr. Cell pellets were resuspended in buffer A (20 mM Tris-HCl, pH 8.0, 500 mM NaCl, 5% glycerol, 20 mM imidazole, 1 mM phenylmethylsulfonyl fluoride), lysed by the EmulsiFlex-C3 homogenizer (Avestin), and centrifuged at 20,000 rpm for 1 hr at 4°C in a JA-20 fixed angle rotor (Avanti J-E series centrifuge, Beckman Coulter). The supernatant containing SpyCas9 protein was loaded to 5 mL HisTrap Fastflow column (GE Healthcare) pre-equilibrated in buffer A and eluted with buffer A supplemented with 480 mM imidazole. The His6-SUMO tag was removed by ULP1 and during dialysis against buffer A and then separated by re-loading to HisTrap column. The flow-through fraction was further dialyzed against buffer B (20 mM Tris-HCl, pH 7.5, 300 mM NaCl, 5 mM  $\beta$ -mercaptoethanol) and loaded on 5 mL HiTrap Heparin HP Sepharose column (GE Healthcare) pre-equilibrated in buffer B and eluted by a linear gradient from 300 mM to 1 M. The recombinant protein was further purified by Superdex 200 16/60 column (GE Healthcare) in buffer C (20 mM HEPES, pH 7.2, 300 mM NaCl, 2 mM MgCl<sub>2</sub>, 5 mM DTT). The relevant fractions were concentrated to 20 mg/ml and flash-frozen in liquid nitrogen and stored in  $-80^{\circ}\text{C}$ .

The genes encoded full-length *acrIIA2* and *acrIIA4* were synthesized and subcloned into a modified pRSF-Duet-1 vector with N-terminal His6-SUMO tag, respectively. The proteins were overexpressed in *Escherichia coli* BL21 (DE3) strain and affinity purified using HisTrap Fast flow column by the same method as described above. After removing the His6-SUMO tag, the flow-through fractions containing the recombinant proteins were concentrated and loaded on Superdex 200 16/60 column pre-equilibrated in buffer E (20 mM HEPES, pH 7.2, 150 mM NaCl, 2 mM MgCl<sub>2</sub>, 5 mM DTT). Different mutations were generated based on PCR-based method. The mutants were purified by the same method as described above. For MBP pull-down assay, the gene encoded SpyCas9 and *acrIIA4* were inserted into a modified pMAL vector with a N-terminal His6-MBP tag following a Tobacco Etch Virus (TEV) cleavage site. The MBP-tagged proteins were purified using HisTrap Fast flow column by the same method as described above.

To assemble the SpyCas9-sgRNA-AcrIIA4 ternary complex, the purified doubly mutated D10A/H840A protein was mixed with sgRNA and AcrIIA4 at the molar ratio of 1:1.1:10 and incubated on ice for 30 min. The reconstituted binary and ternary complexes were purified by gel filtration chromatography on a Superdex 200 10/300 column pre-equilibrated in buffer D (20 mM HEPES, pH 7.2, 200 mM NaCl, 2 mM MgCl<sub>2</sub>, 5 mM DTT).

### Crystallization, Data Collection, and Structure Determination

Crystallization was performed using the hanging drop vapor diffusion method at 20°C. Crystals of SpyCas9-sgRNA-AcrIIA4 ternary complex were grown from drops consisting of 1  $\mu\text{L}$  protein solution (about 8 mg/mL) and 1  $\mu\text{L}$  reservoir solution containing 0.1 M HEPES (pH 7.0), and 15% PEG3350 (v/v). The crystals were cryoprotected by the reservoir solution supplemented with 30% ethylene glycol. The dataset was collected at 100 K at the Advanced Photo Source (APS) at the Argonne National Laboratory. The diffraction data was processed with HKL2000 (Otwinowski and Minor, 1997). The statistics of the diffraction data are summarized in Table 1.

The structure SpyCas9-sgRNA-AcrIIA4 ternary complex was solved by the molecular replacement (MR) method using Phenix (Adams et al., 2002) using SpyCas9-sgRNA binary complex (PDB: 4ZT0) (Jiang et al., 2015) as a search template. AcrIIA4 was manually built by using Coot (Emsley et al., 2010). The structural model was refined using Phenix (Adams et al., 2002). The statistics of the structure refinement and the quality of the final structure model are also summarized in Table 1. All molecular graphics were generated by PyMOL (<http://www.pymol.org>) and CueMol (<http://www.cuemol.org>).

### In Vitro Transcription and Purification of sgRNA

The sgRNA followed by the hammerhead ribozyme was transcribed in vitro using T7 RNA polymerase. Large scale transcription reaction (20 ml) was performed in buffer 100 mM Tris-HCl, pH 7.9, 30 mM DTT, 15 mM MgCl<sub>2</sub>, 2 mM spermidine, 4 mM each NTP, 50  $\mu\text{g}/\text{ml}$  DNA template, 2.5  $\mu\text{g}$  home-made T7 RNA polymerase. The mixture was incubated at 37°C for 3 hr and then supplemented

by  $\text{MgCl}_2$  to final concentration of 50 mM and incubated for another 30 min. The transcribed sgRNA was purified by 10% denaturing TBE-urea PAGE, extracted from gel by electroelution using Elutrap (GE Healthcare), and then further purified by ion-exchange using HiTrap Q Fastflow Sepharose column (GE Healthcare) pre-equilibrated by buffer E (20 mM Tris-HCl, pH 7.0). Elution of sgRNA was achieved by a linear gradient from 0 mM to 1 M NaCl in 20 column volumes. The RNA was denatured at 95°C for 5 min and slowly cooling to room temperature.

Template of sgRNA for in vitro transcription (from 5' to 3'):

GGATAACTCAATTTGTA AAAAAGTTTTAGAGCTAGAAATAGCAAGTTAAAATAAGGCTAGTCCGTTATCAACTTGAAAAAGTGTCTG  
ACGGAGTCTAGACTCCGTCCTGATGAGTCCGTGAGGACGAAACACTTTTTCAAGTTG

### In Vitro Cleavage Assay

The ~600 bp linear target DNA containing the 5'-TGG-3' PAM was synthesized and amplified by PCR. The cleavage reaction was performed by mixing target DNA, sgRNA and SpyCas9 proteins at the molar ratio of 1:1:1, in cleavage buffer (20 mM Tris-HCl, pH 7.5, 100 mM KCl, 5 mM  $\text{MgCl}_2$ , 5 mM DTT, 5% glycerol). AcrIIA2 or AcrIIA4 was added to the reaction system simultaneously. Reaction was performed at 37°C for 15 min and cleaned up by PCR purification columns (Roche) and then run in 10% TBE Urea gel.

Target DNA sequence (from 5' to 3'):

ACCCATGGGAGCAGCTGGTCAGAGGGGACCCCGGCTGGGGCCCCTAACCCCTATGTAGCCTCAGTCTTCCCATCAGGCTCTC  
AGCTCAGCCTGAGTGTTGAGGCCCCAGTGGCTGCTCTGGGGGCCCTCCTGAGTTTCTCATCTGTGCCCTCCCTCCCTGGCCCAG  
GTGAAGGTGTAACTATACTCAATTTGTA AAAAATGTTATTGGCAGAAGCTGGAGGAGGAAGGGCCTGAGTCCGAGCAGAAGAA  
GAAGGGCTCCCATCACATCAACCGGTGGCGCATTGCCACGAAGCAGGCCAATGGGGAGGACATCGATGTCACCTCCAATGACTA  
GGGTGGGCAACCACAAACCCACGAGGGCAGAGTGCTGCTTGTCTGCTGGCCAGGCCCTGCGTGGGCCCAAGCTGGACTCTGG  
CCACTCCCTGGCCAGGCTTTGGGGAGGCCTGGAGTCATGGCCCCACAGGGCTTGAAGCCCGGGGCCGCCATTGACAGAGGGA  
CAAGCAATGGGCTGGCTGAGGCCTGGGACCACTTGGCCTTCTCCTCGGAGAGCCTGCCTGCCTGGGCGGGCCCCGCCGCCAC  
CGCAGCCTCCCAGCTGCTCTCCGTGTCTCCAATCTCCCTTTGTTTTGATGCATTCTGTTTTAATT

PAM is highlighted in bold, and the target sequence is underlined.

### SEC-MALLS

SEC-MALLS experiments were performed by using a Superdex 75 10/300 column (GE Healthcare) and a Shimadzu HPLC System. Protein samples (100  $\mu\text{L}$ ) at a concentration of 2 mg/mL were loaded onto a gel filtration column and eluted with one column volume (24 mL) in buffer E (20 mM HEPES, pH 7.2, 150 mM NaCl, 2 mM  $\text{MgCl}_2$ , 5 mM DTT) at a flow rate of 0.3 mL/min. The eluting fractions were monitored using a DAWN HELEOS-II 18-angle light scattering detector (Wyatt Technologies), a SPD20A UV/Vis detector (Shimadzu), and an Optilab rEX refractive index monitor (Wyatt Technologies). Data were analyzed by using Astra (Wyatt Technologies).

### Size-Exclusion Chromatography Assay

The target and non-target DNA strands were purchased from IDT (Integrated DNA Technologies) and dissolved in buffer consisting of 20 mM Tris-HCl, pH 7.5, 50 mM NaCl. The target and non-target DNA strands were mixed together with a molar ratio of 1:1. The mixture of two DNA strands were denatured at 95°C for 5 min and then annealed by slowly cooling to room temperature. For the assays of the apo-SpyCas9 and AcrIIA2/AcrIIA4, the purified wild-type SpyCas9 and AcrIIA2/AcrIIA4 were mixed at the molar ratio of 1:10 and incubated on ice for 30 min. For the assays of the sgRNA-bound SpyCas9, wild-type SpyCas9, sgRNA, and AcrIIA2/AcrIIA4 were mixed at the molar ratio of 1:1.1:10 and incubated on ice for 30 min. For the assays of the DNA-bound SpyCas9, dSpyCas9, sgRNA, dsDNA and AcrIIA2/AcrIIA4 were mixed at the molar ratio of 1:1.1:1.5:10 and incubated on ice for 30 min. All the mixture was loaded on Superdex 200 10/300 column (GE Healthcare) in buffer D (20 mM HEPES, pH 7.2, 200 mM NaCl, 2 mM  $\text{MgCl}_2$ , 5 mM DTT). The fractions are detected by SDS-PAGE.

### MBP Pull-Down Assay

100  $\mu\text{g}$  MBP-SpyCas9 and 100  $\mu\text{g}$  AcrIIA2/AcrIIA4, in presence or absence of sgRNA (molar ratio, 1:1.1), and 30  $\mu\text{L}$  amylose resin (New England Biolabs) were mixed at 4°C for 1 hr in buffer D (20 mM HEPES, pH 7.2, 200 mM NaCl, 2 mM  $\text{MgCl}_2$ , 5 mM DTT). Alternately, 100  $\mu\text{g}$  MBP-AcrIIA4 and 100  $\mu\text{g}$  SpyCas9, in presence or absence of sgRNA (molar ratio, 1:1.1) and sgRNA-dsDNA (molar ratio, 1:1.1:1.5), and 30  $\mu\text{L}$  amylose resin (NEB) were mixed at 4°C for 1 hr in buffer D. The resin was washed three times using buffer D and detected by SDS-PAGE.

### Electrophoretic Mobility Shift Assay (EMSA)

The purified dSpyCas9 (0.1 nM) and sgRNA at a molar ratio of 1:1.1 were mixed in the absence or presence of dsDNA at a molar ratio of 1:1.5, and then incubated on ice for 30 min in buffer D (20 mM HEPES, pH 7.2, 200 mM NaCl, 2 mM  $\text{MgCl}_2$ , 5 mM DTT) to generate dSpyCas9-sgRNA binary and dSpyCas9-sgRNA-dsDNA ternary complexes. The purified AcrIIA2/AcrIIA4 and dsDNA (molar ratio, 1:1.5) were simultaneously mixed with dSpyCas9-sgRNA binary complex and incubated on ice for 30 min in buffer D. Alternately, the purified AcrIIA2/AcrIIA4 was mixed with dSpyCas9-sgRNA-dsDNA ternary complex and incubated on ice for 30 min in buffer D. The mixture was run on 2% agarose gel at 4°C and visualized by ethidium bromide (Sigma).



## QUANTIFICATION AND STATISTICAL ANALYSIS

In vitro cleavage, SEC-MALLS, SEC, and MBP pull-down experiments were repeated three times, and representative results were shown.

## DATA AND SOFTWARE AVAILABILITY

The atomic coordinate has been deposited in the Protein Data Bank with accession number PDB: 5VW1 (SpyCas9-sgRNA-AcrIIA4 ternary complex). Original unprocessed gel images in this manuscript have been deposited to Mendeley Data and are available at <https://dx.doi.org/10.17632/34cnpysb7k.1>.